Biosensors and Bioelectronics 90 (2017) 336–342

Contents lists available at ScienceDirect

Biosensors and Bioelectronics

journal homepage: www.elsevier.com/locate/bios

Engineering anatase hierarchically cactus-like TiO_2 arrays for photoelectrochemical and visualized sensing platform

Chaomin Gao[a], Yanhu Wang[a], Shuai Yuan[b], Jie Xue[a], Bingqiang Cao[b], Jinghua Yu[a,*]

[a] Key Laboratory of Chemical Sensing & Analysis in Universities of Shandong, University of Jinan, Jinan 250022, PR China
[b] School of Material Science and Engineering, Materials Research Center for Energy and Photoelectrochemical Conversion, University of Jinan, Jinan 250022, PR China

ARTICLE INFO

Keywords:
Anatase hierarchically cactus–like TiO_2
Electrochromic
Prussian blue
Photoelectrochemical
Molecular imprinting technique

ABSTRACT

This work described that one–step synthesis three dimensional anatase hierarchically cactus–like TiO_2 arrays (AHCT) and their application in constructing a novel photoelectrochemical (PEC) and visualized sensing platform based on molecular imprinting technique, which reports its result with the prussian blue (PB) electrode served as the electrochromic indicator for the detection of glycoprotein (RNase B). The AHCT arrays were perpendicularly grown on FTO substrate with tunable sizes, offering many advantages, such as large contact area, rapid charge electron separation and transport. A possible formation process of the interesting AHCT arrays has been investigated based on time–dependent experiment. In addition, the PEC and visualized sensing platform was constructed based on the molecularly imprinted polymer modified AHCT arrays. Specifically, in the proposed system, the more RNase B being, the more insulating layer was formed on the surface of AHCT arrays that impeded the harvesting of light and electron transfer, resulting in the reduction of photocurrent. When upon light illumination, the photogenerated electrons flow through an external circuit to PB, leading to the reduction of PB to prussian white (PW), which is transparent. The rate of decolourization of PB is proportional to the concentration of RNase B. In this way, a visualized PEC sensing platform that gives its quantitative information could be performed by monitoring the change of color intensity. Under optimal conditions, the protocol possessed a detection range of 0.5 pM to 2 μM (r=0.997) and the limit of detection was 0.12 pM toward RNase B. Our method eliminates the need for sophisticated instruments and high detection expenses, making it possible to be a reliable alternative in resource–constrained regions.

1. Introduction

As a promising analytical technique, photoelectrochemical (PEC) sensor has received substantial widespread research interest in quantification of different analytes due to its unmatched merits such as affordable, high sensitivity, simple operation and micromation (Li et al., 2012, 2013; Golub et al., 2009). Furthermore, two separate forms of signal for excitation and detection are usually employed in PEC sensor, featuring it with high sensitivity and a low background signal (Li et al., 2015; Zhang et al., 2014). Undoubtedly, performance of PEC sensor relies heavily on employed photoactive materials, which should possess the merits of improved electron transport and reduced charge recombination. To date, narrow band gap inorganic semiconductor nanomaterials or quantum dots are the most widely utilized photoactive materials (Zhao et al., 2012, 2015; Li et al., 2014; Yang et al., 2015). Titanium dioxide (TiO_2) nanomaterials, with multiple polymorphs such as anatase, brookite and rutile are known for their diverse applications in virtue of their chemical stability, biocompatibility and photoelectric activity (Linsebigler et al., 1995; Li et al., 2012; Zhu et al., 2016). In recent years, one–dimensional (1D) nanostructure TiO_2 has been proved to be an excellent photoactive material to construct PEC sensor, owing to its long axis to absorb light yet a short radial distance for separation of photogenerated charge carriers (Zhu et al., 2016; Tang et al., 2015; Liu et al., 2015). Actually, 1D TiO_2 does satisfy the requirements of improving electron transport, nevertheless, their further enhanced performance is hindered by the insufficient surface area and the considerable free space among adjacent nanowires. In contrast, of particular interests are the well–ordered three dimensional (3D) hierarchically architectures TiO_2, which provide a platform for integration of nanostructures on a larger and more manageable scale into high–performance applications (Wang et al., 2010). Motivated by the fact that the anatase phase of TiO_2 exhibits slower charge recombination rate and better transparency than rutile, (Deb, 2005) tremendous efforts have been dedicated to constructing

* Corresponding author.
E-mail address: ujn.yujh@gmail.com (J. Yu).

http://dx.doi.org/10.1016/j.bios.2016.12.002
Received 29 September 2016; Received in revised form 22 November 2016; Accepted 1 December 2016
Available online 02 December 2016
0956-5663/

3D anatase TiO_2 structures, which could offer a direct transport pathway for charge carriers, enhancing charge transport, improving the charge collection efficiency (Wen et al., 2016). Very recently, our group developed a visible light driven biofuel cell based on 3D branched rutile TiO_2 nanorods, representing another proof–of–concept advance in biosensor (Gao et al., 2016). In addition, Wu et al. reported that high–efficiency dye–sensitized solar cells were constructed based on hierarchical branched TiO_2 which was synthesized via hydrothermal method with $K_2TiO(C_2O_4)_2$ (Wu et al., 2014a, 2014b). Nevertheless, although anatase hierarchical TiO_2 had been prepared and utilized in dye sensitized solar cells (Wu et al., 2014a, 2014b) and lithium ion batteries (Wen et al., 2016), their utilization in constructing performance PEC sensor remain unexplored. In this work, 3D AHCT arrays are successfully synthesized via a facile one–step hydrothermal method and utilized in fabricating visualized PEC sensing for the first time.

Nevertheless, while the PEC sensor exhibits promising, it relied on antibodies to realize the selective recognition, which has some fundamental limitations including tedious screening, high cost and limited stability (Zhang et al., 2015; Holford et al., 2012). Alternative synthetic artificial receptors, molecularly imprinted polymers (MIP), bear predetermined binding cavities and exhibit significant advantages, such as low cost, high stability and potential reusability (Xing et al., 2012; Vlatakis et al., 1993). By integration the specific recognition of MIP and sensitivity of PEC, the selectivity of PEC sensing is remarkably improved. In addition, traditional PEC sensors require the involvement of expensive electrochemical workstation to complete, making the devices depart from miniaturization and portable tendency. Prussian blue (PB), as the electrochromic material, is known to possess excellent electrochromic properties and has a broad absorption in the wavelength range of 600–800 nm, making it a promising electrochromic display (Han et al., 2014). Recently, Crooks et al. reported an electrochemical sensing platform using a PB spot/ITO as the electrochromic indicator for visual detection of glucose and H_2O_2 (Liu and Crooks, 2012). Inspired by this, a novel PEC and visualized sensing platform was constructed by introducing PB/ITO into PEC model. When the PB electrode was connected with the photoelectrode, the generated photoelectrons could be transported to PB electrode through the external circuit and convert PB into its reducing form prussian white (PW). The color of PB electrode was changed from blue to nearly colorless, which could be observed by naked eyes. In this way, by monitoring the change of color intensity, the concentration of RNase B could be obtained.

Glycoproteins play crucial roles in a wide variety of physiological and pathological process, such as protein folding, immune response and tumor cell metastasis (Li et al., 2011). Changes of protein glycosylation could be utilized in early stage diagnostics of some cancers, as well as other diseases (Chandler and Goldman, 2013; Gilgunn et al., 2013). In this study, RNase B, possessing one glycosylation site, to which five high–mannose glycan isoforms may be attached, was selected as the target glycoprotein, and its glycans were utilized as the templates. Essentially, ultrasensitive detection of glycoprotein is crucial for early diagnosis and therapy of many diseases. Therefore, simple, cost–effective and highly sensitive methods for glycoprotein detection are much preferred for clinical diagnostics and therapeutics.

In present work, we describe a facile one–step hydrothermal method for growing AHCT arrays and their application in constructing PEC and visualized sensing for the first time. Desirable morphologies of obtained AHCT arrays could be obtained by varying the experiment parameters, such as reaction time and temperature. The improved electron transport and reduced charge recombination properties of resulting AHCT arrays endow the sensitivity of proposed sensing platform. Intriguingly, by equipped with PB served as electrochromic indicator, a PEC and visualized sensing platform was successfully fabricated. In this way, the concentration of RNase B could be observed only by monitoring the color intensity change of PB.

2. Experimental

2.1. Chemicals

Fluorine–doped tin oxide (FTO) glass substrate with a thickness of 2.2 mm (resistance of $< 15\ \Omega$/sq) was purchased from Xiamen FTO Photoelectricity Industry (Xiamen, China). Ribonuclease A (RNase A), ribonuclease B (RNase B), horseradish peroxidase (HRP), transferrin (TRF), 2,4–difluoro–3–formyl–phenylboronic acid (DFFPBA), tetraethylorthosilicate (TEOS), potassium titanium oxide oxalate dehydrate, diethylene glycol and ammonium hydroxide (28%) were obtained from Sigma–Aldrich (St. Louis, MO, USA). All chemicals were of analytical grade and were used as received. Ultrapure water obtained from a Millipore water purification system (≥18.2 MΩ cm, Milli–Q, Millipore) was used in all assays and solutions.

2.2. Preparation of AHCT arrays on FTO substrate and PB/ITO electrode

Firstly, FTO substrate was cleaned thoroughly by sonication. 0.35 g potassium titanium oxide oxalate dehydrate (PTO) was dispersed in 3 mL ultrapure water, followed by adding 15 mL diethylene glycol (DEG) with stirring for 30 min. After that, the mixture was transferred to a teflon–lined stainless steel autoclave, where the cleaned FTO substrate was placed with the conducting side facing down, sealing and heating at 160 °C for 3–12 h. Finally, the FTO substrate was taken out and rinsed thoroughly with ultrapure water, drying in ambient air at 80 °C, annealing at 450 °C for 2 h.

PB/ITO was prepared according to a previous report with some modification (Jin et al., 2013). Typically, ITO substrate was washed by sonication, then electropolymerizated with PB in a freshly prepared solution, containing 0.1 M KCl, 0.1 M HCl, 2.5 mM $K_3[Fe(CN)_6]$ and 2.5 mM $FeCl_3$, with the potential of 0.4 V for 400 s. The obvious color change of ITO during the process of electropolymerization demonstrated the successful preparation of PB film. Finally, The PB/ITO electrode was thoroughly rinsed with ultrapure water to remove the physically adsorbed species, and then dried in 80 °C overnight.

2.3. Fabrication of the MIP–based PEC and visualized sensing platform

Scheme S1 depicts the fabrication procedures of the visualized PEC sensing platform. The glycan–imprinted DFFPBA/AHCT arrays are synthesized according to the boronate affinity oriented surface imprinting approach reported previously with major modifications (Bi and Liu, 2013; Wang et al., 2014). Firstly, the obtained AHCT arrays were immersed in 10 mL of ultrapure water and then treated with 1.5 mL of 3–Aminopropyltriethoxysilane (APTES) under stirring for 6 h. After that, the AHCT arrays were washed for several times to obtain amino–functionalized sample. Then the resulting AHCT arrays were placed to 20 mL of anhydrous methanol containing 200 mg DFFPBA and 1% (w/w) sodium cyanoborohydride with stirring for 24 h, followed by washing thoroughly with ultrapure water. Then the DFFPBA/AHCT arrays were immersed into 10 mL of 50 mM ammonium bicarbonate containing 600 mM sodium chloride buffer solution (pH 8.5) and 100 μL of RNase B glycans stock solution, stirring for 2 h. 50 mM ammonium bicarbonate buffer solution (pH 8.5) was utilized to wash the modified electrode. To imprint glycans on the DFFPBA/AHCT arrays, the modified electrode was immersed into 160 mL anhydrous ethanol containing 2.8 mL ammonium hydroxide. Then 40 mL of TEOS in anhydrous ethanol (10 mM) was added and the mixture was gently stirred for 50 min (Bie et al., 2015). Finally, the RNase B glycan–imprinted DFFPBA/AHCT arrays were washed with ethanol for three times. The MIP modified electrode was immersed into 20 mL of 100 mM acetic acid with stirring for 30 min to remove the templates (Bie et al., 2015). Then the molecularly imprinted PEC sensing with

empty sites for RNase B recognition was obtained. Fabrication processes of non–imprinted DFFPBA/AHCT arrays were as same as the approach mentioned above but without the addition of template.

2.4. Photoelectrochemical measurement

The details assay procedures of the visualized PEC sensing platform are described as follows. 20 μL samples containing different concentrations of RNase B were added onto the electrode surface, and allowed to be absorbed for 40 min to reach the equilibrium binding, followed by washing to prevent non–specific binding. Then, the electrode was connected to PB electrode and both were placed in PBS (pH 7.4, 0.1 M) containing glucose (40 mM), which acted as a sacrificial electron donor. A 500 W Xe lamp was used as irradiation source. The PB electrode, whose color became weak gradually, was taken out and the absorbance was measured after the light irradiation for 10 s. The decolourization of PB could be easily observed with naked eyes. In addition, the visual photographs of the experimental facility of proposed visualized PEC sensing platform were shown in Fig. S1.

3. Results and discussion

3.1. Characterization of the AHCT arrays and PB/ITO electrode

Fig. 1 exhibits the characterizations of obtained AHCT arrays grown vertically on FTO substrate. Fig. 1A reveals that AHCT arrays are hierarchical structure, composing of slender TiO_2 nanoflakes (NFs) backbone covered by large amount of short distinct TiO_2 nanorods branches. The SEM of MIP modified AHCT arrays are shown in Fig. S2.

Transmission electron microscopy (TEM) characterizations of the resulting AHCT arrays are carried out, as shown in Fig. 1B. As seen, a layer of density branches with length of around 200 nm are uniformly covered on the surface of TiO_2 NF backbone, which could enhanced the light scattering capability of the samples. Moreover, high–resolution TEM images of TiO_2 NF and a single branch exhibit the single crystalline nature (inset of Fig. 1B), with lattice spacing of 0.35 nm, consistent with the (101) plane of the anatase TiO_2 structure. In addition, the phase structure of the sample is also characterized by XRD measurement, as shown in Fig. 1C. The diffraction peaks of the AHCT arrays are consistent with the anatase phase (JCPDS card No. 21–1272) (Wu et al., 2014a, 2014b), which is in good concurrence with the result of HRTEM. Phase structure of the sample is further measured by Raman spectra, showing in Fig. 1D. As seen, the vibrational modes at 145, 198, 395, 516, and 637 cm^{-1} exhibit the characteristic Raman bands of single anatase phase, which further demonstrate that the as–prepared sample is single crystal anatase TiO_2 structure (Cao et al., 2016).

Fig. 2A reveals a highly dense PB film with rough but uniform film on the surface of ITO electrode, implying the PB has been successfully prepared. Meanwhile, as seen from the visual photograph of the

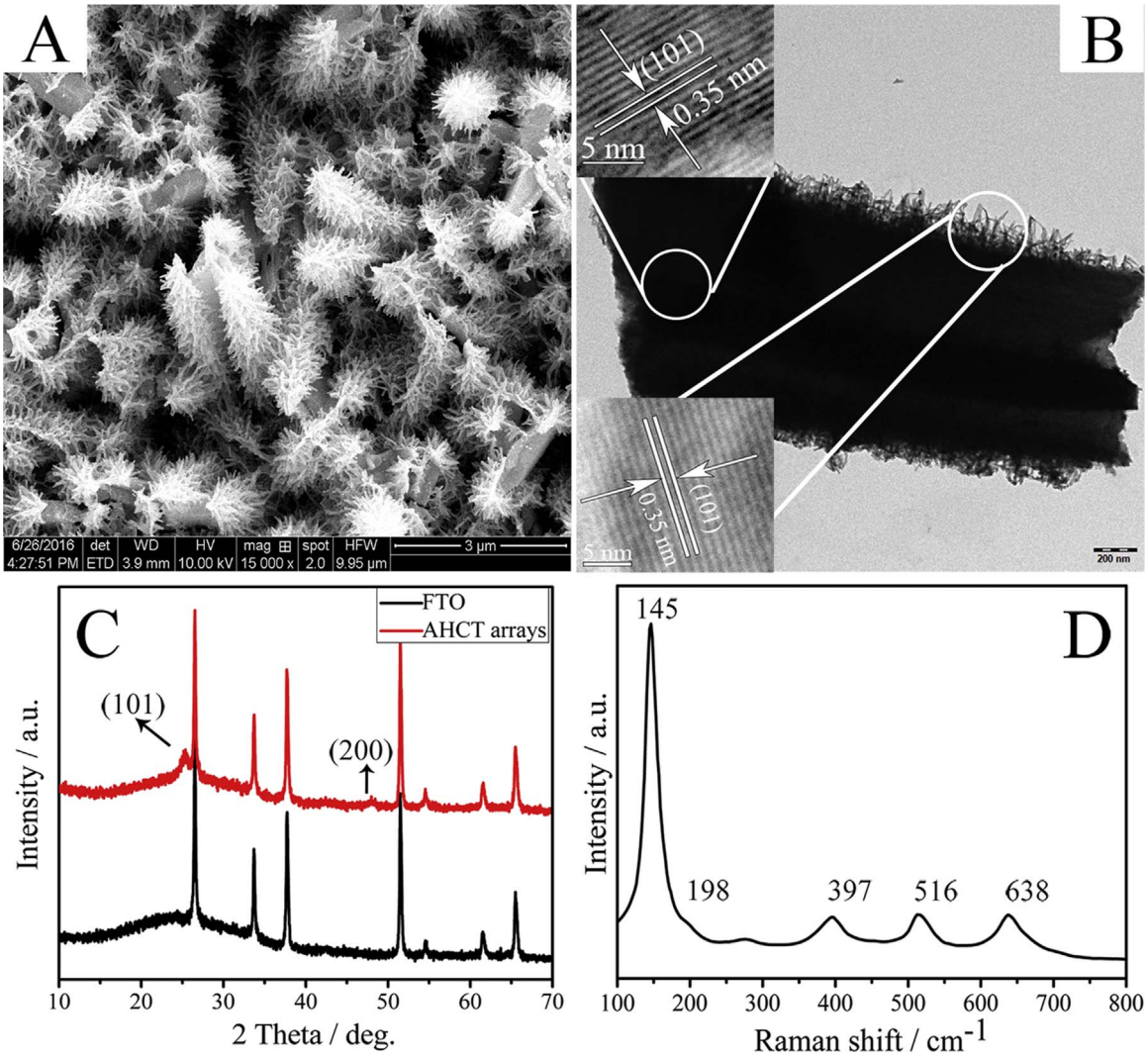

Fig. 1. SEM (A), low magnification TEM image (B), XRD (C), and (D) Raman of AHCT arrays. The insets of (B) are the high–resolution TEM images of TiO_2 NFs and AHCT arrays.

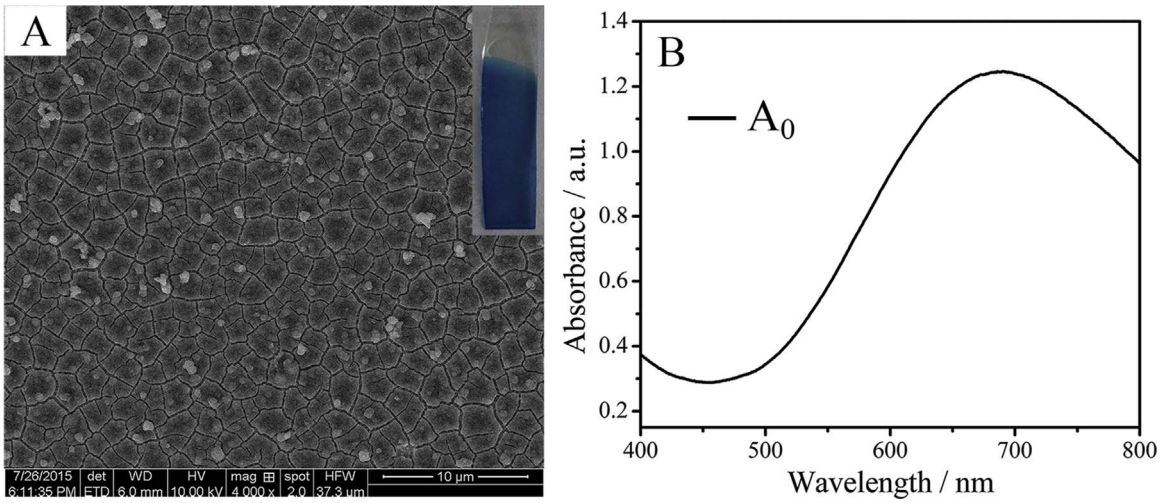

Fig. 2. SEM image (A) and UV–Vis absorption spectra of PB (B). The inset of (A) is visual photograph of PB film. (For interpretation of the references to color in this figure legend, the reader is referred to the web version of this article.)

obtained PB film, obvious blue color could be observed on the ITO (Fig. 2A inset). As shown in Fig. 2B, a broad absorption band in the wavelength range of 600–800 nm also demonstrates the successful preparation of PB/ITO, making the proposed visual system possibility. In addition, the initial absorbance of PB is denoted as A_0.

3.2. Growth mechanism of resulting AHCT arrays

After determining the structural characteristics and composition of the as–prepared AHCT arrays, time–dependent experiments are carried out to explore the one–step growth mechanism. SEM images harvested at different periods during the hydrothermal reaction are shown in Fig. 3. At 3 h, oriented short and small TiO_2 NFs are covered on FTO substrate, as depicted in Fig. 3A. The TiO_2 NFs become numerous and longer after 4 h of hydrothermal growth (Fig. 3B). Then tiny TiO_2 nanobranches begin to germinate on the surface of TiO_2 NFs, making the surface of TiO_2 NFs become rough (Fig. 3C) when the reaction time is 5 h. The needle–shaped branches nanostructures are conspicuous and uniformly distributed on the entire edge of TiO_2 NFs backbone (Fig. 3D) with the reaction time of 6 h. When the time prolongs to 8 h, the branches become more numerous and longer, which could greatly enhance the filling rate in the intervals of neighbouring NFs (Fig. 3E). With this reaction time, the novel AHCT arrays consisting of TiO_2 NFs backbone and short branches are

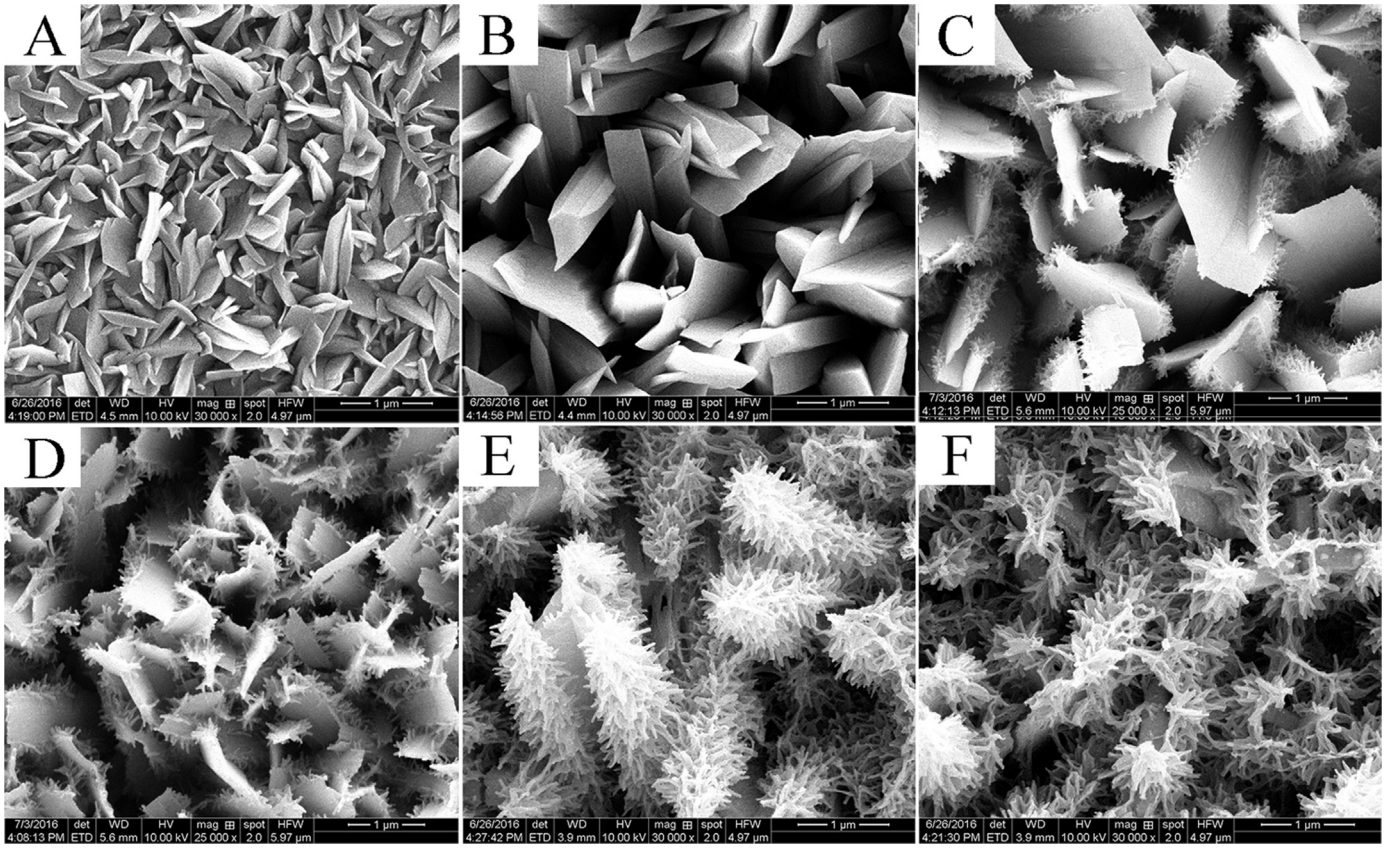

Fig. 3. Time–dependent growth process of AHCT arrays. Typical SEM images of the sample grown with the different reaction time: (A) 3 h, (B) 4 h, (C) 5 h, (D) 6 h, (E) 8 h, (F) 12 h.

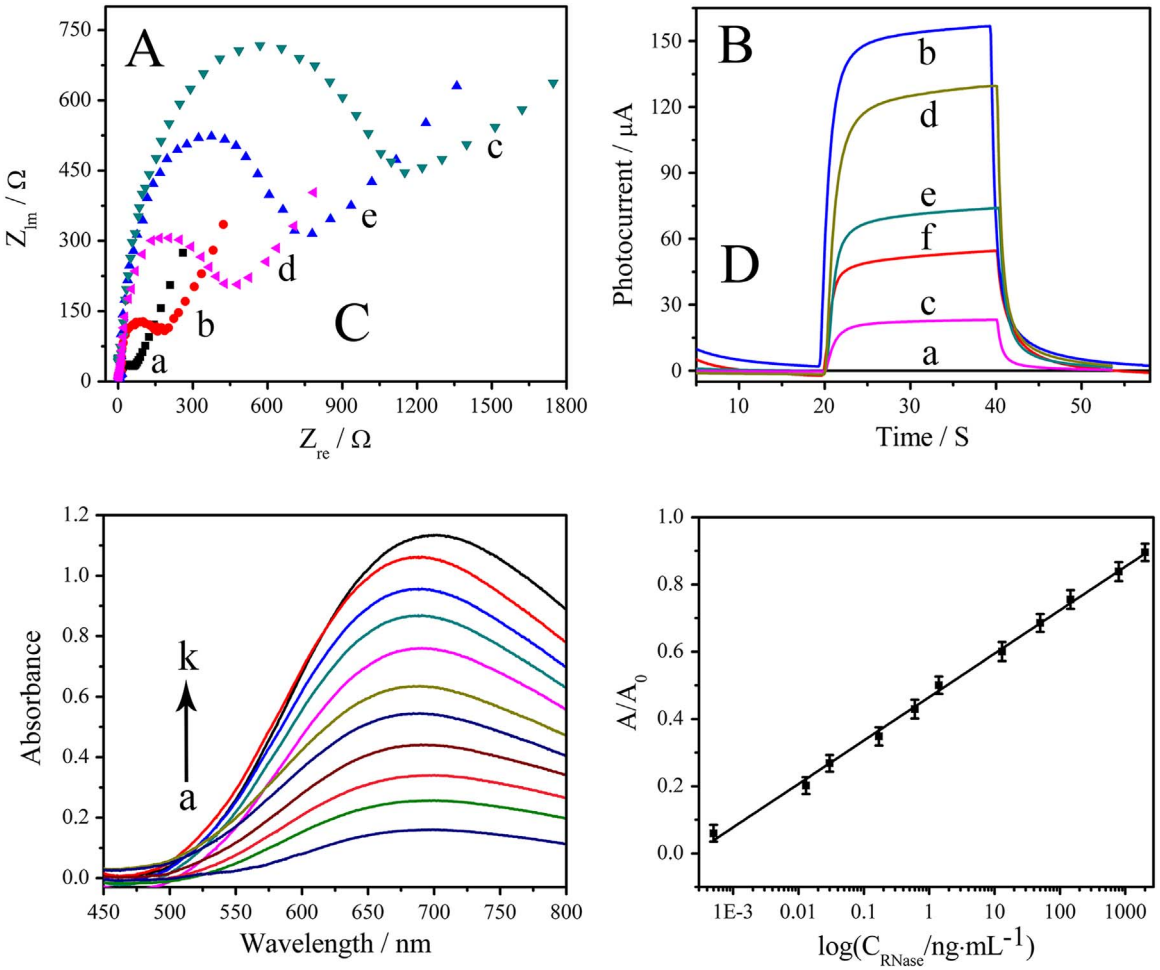

Fig. 4. (A) EIS of bare FTO (a), after AHCT arrays modification (b), after MIP immobilization (c), after removal of glycan (d), after incubation with 10 nM RNase B (e); (B) photocurrent responses of FTO electrode (a), AHCT arrays electrode (b), MIP modified AHCT arrays electrode (c), removal of template (d), removal of template and addition of 10 nM (e) and 100 nM (f) of RNase B solution; (C) Ultraviolet absorption spectra of PB electrode when connected with photoelectrode in different concentrations of RNase B under UV light irradiation (the concentration was increasing from a to j); (D) The relationship between A/A0 and RNase B concentrations.

successfully achieved. As seen from Fig. 3F, when the time is 12 h, excessive precursor continues to deposit on the AHCT arrays and it is difficult to distinguish the branched structure. In addition, the PEC property of AHCT arrays harvested at different reaction time has been investigated, as shown in Fig. S4. It could be seen that the photocurrent is the highest when the reaction time is 8 h.

3.3. Electrochemical and PEC characteristics of MIP-AHCT arrays electrode

Electrochemical impedance spectroscopy (EIS) is an effective means to characterize the interface properties of modified electrode (Chen et al., 2008). In this work, EIS is measured in the frequency range 100 MHz to 10 KHz, with the phosphate buffer solution (PBS, 0.1 M, pH 7.4) containing 5 mM $[Fe(CN)_6]^{3-/4-}$ as probe. In EIS spectra, the diameter of the semicircle at higher frequencies equals the electron–transfer resistance (R_{et}), controlling the electron transfer kinetics of the redox probe at the electrode interface. As shown in Fig. 4A, the impedance spectrum of the bare FTO exhibits a small R_{et} (curve a). After AHCT arrays and insulating MIP layer are successively immobilized onto the electrode, the R_{et} exhibits an obvious increase owing to weak conductivity of semiconductor and insulating property of MIP layer (curve b, c). The decrease of R_{et} from curve d to curve c could be attributed to the removal of template from the MIP layer and thus the unoccupied binding cavities in the MIP layer are available for the hexacyanoferrate redox probe to diffuse through. As seen in curve e, the R_{et} increases compared with curve d when 10 nM RNase B was added, implying the successfully preparation of the MIP based AHCT arrays.

The sensor developing process is also monitored by stepwise transient photocurrent responses upon the intermittent light irradiation with the results displays in Fig. 4B. As seen, almost no photocurrent is observed from FTO electrode (curve a). When modified with AHCT arrays, which own great photoelectric converting performance, the photocurrent is increased remarkably (curve b). After anchoring the MIP, the photocurrent decreased considerably (curve c), attributing to the polymer film modified on the surface of AHCT arrays generating an insulating layer which partly hinder the harvesting of light and electron transfer. Furthermore, when removal of the template, the photocurrent increases remarkably due to the more harvesting light of AHCT arrays (curve d). Meanwhile, when the template was removed and then 10 nM (curve e) and 100 nM (curve f) of template was added, the photocurrent of AHCT arrays–MIP decreases with the increasing of the concentration of RNase B, proving that it is possible to sensitively detect RNase B in the proposed PEC sensing platform.

3.4. Possible working principle of the PEC and visualized sensing platform

Scheme 1 depicts the probable working principle of the PEC and visualized sensor. Typically, upon irradiation by UV light, the AHCT arrays could generate a number of electron–hole pairs (Eqs. (1)–(3)).

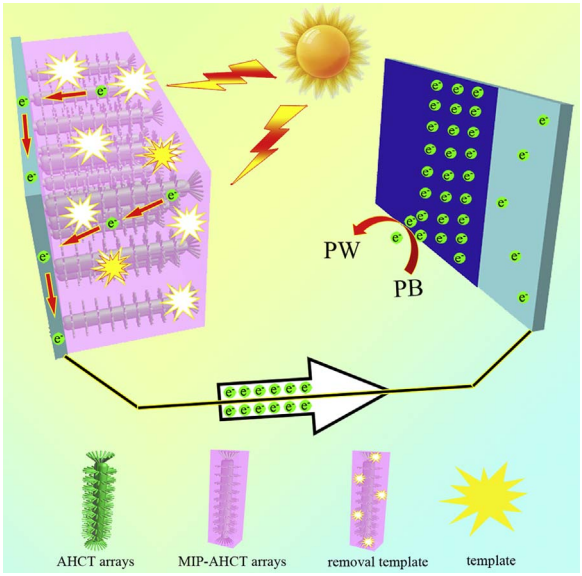

Scheme 1. General working principle of the proposed visualized PEC sensing platform.

Given that TiO_2 possess suitable band structures, photogenerated holes could oxidize glucose to gluconolactone while photogenerated electrons transferred through an external circuit to the PB display electrode, reducing PB to prussian white (PW). Meanwhile the corresponding blue color becomes fade gradually and the absorbance of the PB is measured. Upon continue UV light illumination for 10 s, decreased absorbance is observed because the reduction of Fe(III) in PB resulted in the elimination of the intervalence charge transfer from Fe(III) to Fe(II) causing its absorbance (Bai et al., 2013). Once the RNase B is added, some binding cavities of the MIPs could be occupied, leading to the few light illuminate on the AHCT arrays, so the few photogenerated electrons flow to PB electrode. As the decreasing of the concentration of RNase B, the color fading of PB is obviously observed with naked eyes. Specifically, the color intensity of PB is dependent on the concentration of RNase B. In this case, the RNase B could be detected only by measuring the change of absorbance of PB without needing external power source in a visualized way. All of the processes are illustrated in the following Eqs. (1)–(3):

$$\text{AHCT arrays} + h\nu \rightarrow e^{-}(\text{AHCT arrays}) + h^{+}(\text{AHCT arrays}) \quad (1)$$

$$h^{+}(\text{AHCT arrays}) + \text{glucose} \rightarrow \text{gluconolactone} + H^{+} \quad (2)$$

$$e^{-}(\text{AHCT arrays}) + \text{PB} \rightarrow \text{PW} \quad (3)$$

3.5. Optimization of the sensing conditions

In this work, the glucose was exploited as an efficient electron donor for scavenging photogenerated holes, and the concentration could influence the photocurrent of AHCT arrays. As shown in Fig. S3A, when the glucose concentration was no more than 40 mM, the photocurrent intensity increased gradually with increasing glucose concentration; however, when the concentration was higher than 40 mM no obvious increase in photocurrent intensity was observed. Therefore, the 40 mM was selected as the optimal concentration and used in the further study.

Other experimental conditions were also optimized. The time of removing template and the absorption time of RNase B were important parameters to enhance the sensitivity of the sensor. 40 min and 50 min were chosen as the removing and absorption time, respectively (Figs. S3B and S3C).

3.6. Analytical performance of the visualized PEC sensing platform

The analytical performance of this sensing platform is verified through the detection of RNase B in standard RNase B solution with various concentrations after the addition of 40 mM glucose (in pH=7.4, 0.1 M PBS). As depicts in Fig. 4C, the absorbance intensity of PB increases gradually as the RNase B concentration increasing, which implies the feasibility of RNase B detection. Fig. 4D indicates the relationship between absorbance and RNase B concentration. The ratios of A/A_0 display a good linear correlation with RNase B concentrations over the range of 0.5 pM to 2 μM with a correlation coefficient of 0.997 and a linear equation of $A/A_0=0.47-0.13\log C_{\text{RNase B}}$ (ng mL^{-1}). The limit of detection at a signal–to–noise ratio of 3 for RNase B was 0.1 pM. Here, A_0 is the absorbance intensity of original PB electrode served as the contrast to enhance the accuracy.

3.7. Application in analysis of serum samples

The analytical reliability and application potential of this sensing platform for clinical application was investigated with several real samples of human serum using the proposed method as well as the reference values were obtained from Shandong standard test technology CO., LTD using high performance liquid chromatography (HPLC). If the levels of RNase B were over the calibration ranges, samples could be appropriately diluted prior to assay. The results gave the relative errors less than 5.0%, showing an acceptable agreement between the two methods (Table 1). The detection result indicates the acceptable accuracy and the great potential applicability of prepared sensor for RNase B analysis.

3.8. Stability, reproducibility, and selectivity of the sensing platform

When the sensing platform is dried and stored over four weeks, no apparent change in signal response with the same RNase B concentration (10 nM) is found, illustrating its acceptable long term storage stability (Fig. S4B). The reproducibility of this sensing platform is evaluated by an interassay of analyzing RNase B with five electrodes, and a relative standard deviation of 7.9% is obtained, suggesting that this sensing platform has satisfied reproducibility (Table S1). The selectivity of this sensing platform is assessed by testing its tolerance to a high concentration of functional and structural interfering analogues, such as ribonuclease A (RNase A), transferrin (TRF), and horseradish peroxidase (HRP). The result is listed in Fig. S3D. RNase B coexisted with these interfering agents, no apparent signal change took place in comparison with that of only RNase B even when the concentration of interfering substances are 100 times that of RNase B, suggesting that the sensing platform is sufficiently selective for the detection of RNase B.

4. Conclusion

In summary, a PEC and visualized sensing platform was established by integrating the molecular imprinting technique, equipping the PB

Table 1
Comparison assay results of real samples for the proposed method and referenced method.

Sample	Proposed method (nM)[a]	Reference method (nM)	Relative deviation (%)
1	12.3	11.8	4.24
2	43.5	44.6	−2.47
3	86.8	84.1	3.21
4	120.9	116.2	4.04
5	180.7	177.1	2.03

[a] The average value of seven successive determinations.

electrode as the electrochromic display for RNase B sensitive detection. The sensing mechanism of proposed visualized PEC platform was that monitoring the variation of absorbance of PB, which was proportionally to the amount of RNase B. The absorbance of PB was decreased with the decreasing concentration of RNase B, providing the basis for RNase B detection. In addition, the color fading of PB was easy to be observed by naked eyes and the visual target detection was achieved. Upon proper experimental conditions, the protocol possessed a detection range from 0.5 pM to 2 μM (r=0.997) and the limit of detection was as low as 0.12 pM. Moreover, introducing the electrochromic display into PEC might provide a wide potential application in biochemical sensing and biomedical application.

Acknowledgments

This work was financially supported by National High–tech R & D Program (863 Program) (2015AA034701), and Natural Science Foundation of Shandong Province, China (ZR2014EMP010, and ZR2015JL006).

Appendix A. Supporting information

Supplementary data associated with this article can be found in the online version at doi:10.1016/j.bios.2016.12.002.

References

Bai, L., Jin, L., Han, L., Dong, S.J., 2013. Energy Environ. Sci. 6, 3015–3021.
Bi, X., Liu, Z., 2013. Anal. Chem. 86, 959–966.
Bie, Z.J., Chen, Y., Ye, J., Wang, S.S., Liu, Z., 2015. Angew. Chem. Int. Ed. 54, 10211–10215.
Cao, F.R., Xiong, J., Wu, F.L., Liu, Q., Shi, Z.W., Yu, Y.H., Wang, X.D., Li, L., 2016. ACS Appl. Mater. Interfaces 8, 12239–12245.
Chandler, K., Goldman, R., 2013. Mol. Cell. Proteom. 12, 836–845.
Chen, X.J., Wang, Y.Y., Zhou, J.J., Yan, W., Li, X.H., Zhu, J.J., 2008. Anal. Chem. 80, 2133–2140.
Deb, S.K., 2005. Sol. Energy Mater. Sol. Cells 88, 1–10.
Gao, C.M., Zhang, L.N., Wang, Y.H., Yu, J.H., Song, X.R., 2016. Biosens. Bioelectron. 83, 327–333.
Golub, E., Pelossof, G., Freeman, R., Zhang, H., Willner, I., 2009. Anal. Chem. 81, 9291–9298.
Gilgunn, S., Conroy, P.J., Saldova, R., Rudd, P.M., O'Kennedy, R.J., 2013. Nat. Rev. Urol. 10, 99–107.
Han, L., Bai, L., Dong, S.J., 2014. Chem. Commun. 50, 802–804.
Holford, T.R.J., Davis, F., Higson, S.P.J., 2012. Biosens. Bioelectron. 34, 12–24.
Jin, L., Fang, Y., Shang, L., Liu, Y., Li, J., Wang, L., Hu, P., Dong, S.J., 2013. Chem. Commun. 49, 243–245.
Li, H.N., Mu, Y.W., Yan, J.R., Cui, D.M., Ou, W.J., Wan, Y.K., Liu, S.Q., 2015. Anal. Chem. 87, 2007–2015.
Li, Y.J., Ma, M.J., Zhu, J.J., 2012. Anal. Chem. 84, 10492–10499.
Li, Y.J., Ma, M.J., Yin, G., Kong, Y., Zhu, J.J., 2013. Chem. Eur. J. 19, 4496–4505.
Li, W., Sheng, P.T., Cai, J., Feng, H.Y., Cai, Q.Y., 2014. Biosens. Bioelectron. 61, 209–214.
Linsebigler, A.L., Lu, G., Yates, J.T., 1995. Chem. Rev. 95, 735–758.
Liu, S.Q., Tang, Z.R., Sun, Y.G., Colmenares, J.C., Xu, Y.J., 2015. Chem. Soc. Rev. 44, 5053–5075.
Liu, H., Crooks, R.M., 2012. Anal. Chem. 84, 2528–2532.
Li, Y., Tao, S.C., Steven, B.G., Liu, A.Y., Chan, D.W., Zhu, H., Zhang, H., 2011. Anal. Chem. 83, 8509–8516.
Tang, J., Li, J., Da, P.M., Wang, Y.C., Zheng, G.F., 2015. Chem. Eur. J. 21, 11288–11299.
Vlatakis, G., Andersson, L.I., Muller, R., Mosbach, K., 1993. Nature 361, 645–647.
Wang, C.X., Yin, L.W., Zhang, L.Y., Qi, Y.X., Lu, N., Liu, N.N., 2010. Langmuir 26, 12841–12848.
Wang, S., Ye, J., Bie, Z., Liu, Z., 2014. Chem. Sci. 5, 1135–1140.
Wen, W., Wu, J.M., Jiang, Y.Z., Bai, J.Q., Lai, L.L., 2016. J. Mater. Chem. A 4, 10593–10600.
Wu, W.Q., Xu, Y.F., Rao, H.S., Su, C.Y., Kuang, D.B., 2014a. J. Am. Chem. Soc. 136, 6437–6445.
Wu, W.Q., Rao, H.S., Feng, H.L., Chen, H.Y., Kuang, D.B., Su, C.Y., 2014b. Nano Energy 9, 15–24.
Xing, X.R., Liu, S., Yu, J.H., Lian, W.J., Huang, J.D., 2012. Biosens. Bioelectron. 31, 277–283.
Yang, J.J., Gao, P.C., Liu, Y.X., Li, R.X., Ma, H.M., Du, B., Wei, Q., 2015. Biosens. Bioelectron. 64, 13–18.
Zhang, X.R., Liu, M.S., Mao, Y.N., Xu, Y.P., Niu, S.Y., 2014. Biosens. Bioelectron. 59, 21–27.
Zhao, W.W., Dong, X.Y., Wang, J., Kong, F.Y., Xu, J.J., Chen, H.Y., 2012. Chem. Commun. 48, 5253–5255.
Zhao, W.W., Han, Y.M., Zhu, Y.C., Zhang, N., Xu, J.J., Chen, H.Y., 2015. Anal. Chem. 87, 5496–5499.
Zhu, H., Fan, G.C., Abdel-Halim, E.S., Zhang, J.R., Zhu, J.J., 2016. Biosens. Bioelectron. 77, 339–346.
Zhang, Z., Guan, Y., Li, M., Zhao, A., Ren, J., Qu, X., 2015. Chem. Sci. 6, 2822–2826.